The Scientific Measurement System of the Gravity Recovery and Interior Laboratory (GRAIL) Mission

Citation: Asmar, Sami W. et al. "The Scientific Measurement System of the Gravity Recovery and Interior Laboratory (GRAIL) Mission." Space Science Reviews 178.1 (2013): 25–55.

As Published: http://dx.doi.org/10.1007/s11214-013-9962-0

Publisher: Springer Netherlands

Persistent URL: http://hdl.handle.net/1721.1/107472

Version: Author's final manuscript: final author's manuscript post peer review, without publisher's formatting or copy editing

Space Sci Rev (2013) 178:25–55
DOI 10.1007/s11214-013-9962-0

The Scientific Measurement System of the Gravity Recovery and Interior Laboratory (GRAIL) Mission

Sami W. Asmar · Alexander S. Konopliv · Michael M. Watkins · James G. Williams · Ryan S. Park · Gerhard Kruizinga · Meegyeong Paik · Dah-Ning Yuan · Eugene Fahnestock · Dmitry Strekalov · Nate Harvey · Wenwen Lu · Daniel Kahan · Kamal Oudrhiri · David E. Smith · Maria T. Zuber

Received: 5 October 2012 / Accepted: 22 January 2013 / Published online: 21 February 2013

Abstract The Gravity Recovery and Interior Laboratory (GRAIL) mission to the Moon utilized an integrated scientific measurement system comprised of flight, ground, mission, and data system elements in order to meet the end-to-end performance required to achieve its scientific objectives. Modeling and simulation efforts were carried out early in the mission that influenced and optimized the design, implementation, and testing of these elements. Because the two prime scientific observables, range between the two spacecraft and range rates between each spacecraft and ground stations, can be affected by the performance of any element of the mission, we treated every element as part of an extended science instrument, a science system. All simulations and modeling took into account the design and configuration of each element to compute the expected performance and error budgets. In the process, scientific requirements were converted to engineering specifications that became the primary drivers for development and testing. Extensive simulations demonstrated that the scientific objectives could in most cases be met with significant margin. Errors are grouped into dynamic or kinematic sources and the largest source of non-gravitational error comes from spacecraft thermal radiation. With all error models included, the baseline solution shows that estimation of the lunar gravity field is robust against both dynamic and kinematic errors and a nominal field of degree 300 or better could be achieved according to the scaled Kaula rule for the Moon. The core signature is more sensitive to modeling errors and can be recovered with a small margin.

Keywords Gravity · Moon · Remote sensing · Spacecraft

Acronyms and Abbreviations

AGC	Automatic Gain Control

S.W. Asmar (✉) · A.S. Konopliv · M.M. Watkins · J.G. Williams · R.S. Park · G. Kruizinga · M. Paik · D.-N. Yuan · E. Fahnestock · D. Strekalov · N. Harvey · W. Lu · D. Kahan · K. Oudrhiri
Jet Propulsion Laboratory, California Institute of Technology, Pasadena, CA 91109, USA
e-mail: sami.asmar@jpl.nasa.gov

D.E. Smith · M.T. Zuber
Department of Earth, Atmospheric and Planetary Sciences, Massachusetts Institute of Technology, Cambridge, MA 02139-4307, USA

AMD	Angular Momentum Desaturation
C&DH	Command & Data Handler
CBE	Current Best Estimate
CG	Center of Gravity
CPU	Central Processing Unit
DSN	Deep Space Network
DOWR	Dual One-way Range
ECM	Eccentricity Correction Maneuver
EOP	Earth Orientation Platform
ET	Ephemeris Time
GPS	Global Positioning System
GR-A	GRAIL-A Spacecraft (Ebb)
GR-B	GRAIL-B Spacecraft (Flow)
GRACE	Gravity Recovery and Climate Experiment
GRAIL	Gravity Recovery and Interior Laboratory
GSFC	Goddard Space Flight Center
ICRF	International Celestial Reference Frame
IERS	International Earth Rotation and Reference Systems Service
IR	Infra Red
IPU	Instrument Processing Unit (GRACE mission)
JPL	Jet Propulsion Laboratory
KBR	Ka-Band Ranging
KBRR	Ka-Band Range-Rate
LGRS	Lunar Gravity Ranging System
LLR	Lunar Laser Ranging
LOI	Lunar Orbit Insertion
LOS	Line of Sight
LP	Lunar Prospector
mGal	milliGal (where 1 Gal $= 0.01\ \mathrm{m\,s^{-2}}$)
MGS	Mars Global Surveyor
MIT	Massachusetts Institute of Technology
MOS	Mission Operations System
MIRAGE	Multiple Interferometric Ranging and GPS Ensemble
MMDOM	Multi-mission Distributed Object Manager
MONTE	Mission-analysis, Operations, and Navigation Toolkit Environment
MPST	Mission Planning and Sequence Team
MRO	Mars Reconnaissance Orbiter
MWA	Microwave Assembly
NASA	National Aeronautics and Space Administration
ODP	Orbit Determination Program
OPR	Orbital Period Reduction
OSC	Onboard Spacecraft Clocks
OTM	Orbit Trim Maneuver
PDS	Planetary Data System
PM	Primary Mission
PPS	Pulse Per Second
RSB	Radio Science Beacon
RSR	Radio Science Receiver
SCT	Spacecraft Team

SDS	Science Data System
SIS	Software Interface Specification
SRIF	Square Root Information Filter
SRP	Solar Radiation Pressure
TAI	International Atomic Time
TCM	Trajectory Correction Maneuver
TDB	Barycentric Dynamic Time
TDS	Telemetry Delivery System
TDT	Terrestrial Dynamic Time
TLC	Trans-Lunar Cruise
TSF	Transition to Science Formation
TSM	Transition to Science Maneuver
TTS	Time Transfer System
USO	Ultra-stable Oscillator
UTC	Universal Time Coordinated
VLBI	Very Long Baseline Interferometry

1 Introduction and Heritage

The Gravity Recovery and Interior Laboratory (GRAIL) mission is comprised of two spacecraft, named Ebb and Flow, flying in precision formation around the Moon. The mission's purpose is to recover the lunar gravitational field in order to investigate the interior structure of the Moon from the crust to the core. The spacecraft were launched together on September 10, 2011 and began science operations and data acquisition on March 1, 2012. Zuber et al. (2013, this issue) presents an overview of the mission including scientific objectives and measurement requirements. Klipstein et al. (2013, this issue) describes the design and implementation of the GRAIL payload. Hoffman (2009) described GRAIL's flight system and Roncoli and Fujii (2010) described the mission design.

This paper illustrates how a team of scientists and engineers prepared to meet GRAIL scientific objectives and data quality requirements through simulations and modeling of the design and configuration of the flight and ground systems. It details dynamic and kinematic models for estimating error sources in the form of non-gravitational forces and how these models were applied, along with the lunar gravity model, to elaborate computer simulations in the context of an integrated scientific measurement system. This paper also documents the methods, tools, and results of the simulations. This work was carried out at the Jet Propulsion Laboratory (JPL) prior to the science orbital phase and reviewed by expert peers from different institutions; the knowledge is based on the combined experiences of the team members with gravity observations on numerous planetary missions. This effort demonstrated that the mission was capable of meeting the science requirements as well as paved the way to the operational tools and procedures for the actual science data analysis.

The GRAIL concept was derived from the Gravity Recovery and Climate Experiment (GRACE) Earth mission and utilized a modified GRACE payload called the Lunar Gravity Ranging System (LGRS); the GRAIL and GRACE spacecraft are unrelated. For an overview of the GRACE mission see Tapley et al. (2004a, 2004b); for a description of the GRACE payload, see Dunn et al. (2003); and for error analysis in the GRACE system and measurements, see Kim and Tapley (2002).

Despite the high heritage, there are significant differences between the GRAIL and GRACE science payloads, listed in Table 1. GRACE is equipped with a Global Positioning

Table 1 Functional differences between the GRAIL and GRACE Missions

	GRAIL	GRACE
Target body	Moon	Earth
Launch vehicle	Delta II, USA	Rockot, Russia
Nominal prime mission duration	3 months	5 years
Orbiter mass (kg)	313	487
Launch date	9/10/11	3/17/02
Prime mission mean orbital altitude (km)	55	470
Gravity coefficients	420	120
Timing synchronization method	RSB	GPS
Science-quality accelerometer	N	Y
Adjustable mass for accelerometer at CG	N	Y
Center of gravity calibrations for antenna	Y	Y
Inter-spacecraft links	Ka-/S-band	Ka-/K-band
Spacecraft separation distance (km)	85–225	170–270
Attitude control	Reaction wheels	Magnetic torque
Thrusters gas	Hydrazine	Nitrogen
Star cameras per spacecraft	1	2
Science processor	Single String	Redundant
Star camera software host	C&DH[a]	IPU[b]
USOs per spacecraft	1	2
Absolute timing accuracy	DSN: millisecond	GPS: nanosecond
Relative timing accuracy	TTS: picosecond	GPS: picosecond
Communication stations	DSN	German stations

[a]C&DH is GRAIL's Command and Data Handling Subsystem.

[b]IPU is GRACE's Instrument Processing Unit.

System (GPS) receiver for timing synchronization, and accelerometers for non-gravitational force calibrations, while GRAIL is not. Furthermore, GRACE inter-spacecraft ranging utilizes two radio links at K- and Ka-bands (∼26 GHz and ∼32 GHz, respectively) in order to calibrate the effects of charged particles in the Earth ionosphere, while GRAIL utilizes only one Ka-band link. In lieu of GPS time synchronization, which is not available at the Moon, GRAIL introduced two elements, a second inter-spacecraft link at S-band (∼2.3 GHz) for a Time Transfer System (TTS), and a one-way X-band (∼8.4 GHz) link transmitted from each spacecraft's Radio Science Beacon (RSB) to the Deep Space Network (DSN) stations. With these differences, the GRAIL observable time tagging and synchronization is handled differently from the GRACE GPS-based system as will be discussed below.

Furthermore, while the GRACE observables are referenced to a geocentric frame, GRAIL measurements are referenced to Ephemeris Time (ET) and the solar system barycentric frame of Barycentric Dynamic Time (TDB). Finally, since GRAIL does not carry an accelerometer, attention was given in the design, assembly, and testing of the spacecraft system in order to minimize on the non-gravitational forces acting on the spacecraft, including the solar radiation pressure, lunar albedo and spacecraft outgassing.

All radio signals in the science payload, illustrated in Fig. 1, the Ka-band inter-spacecraft link, the S-band TTS inter-spacecraft link, and the X-band RSB link to Earth, are referenced

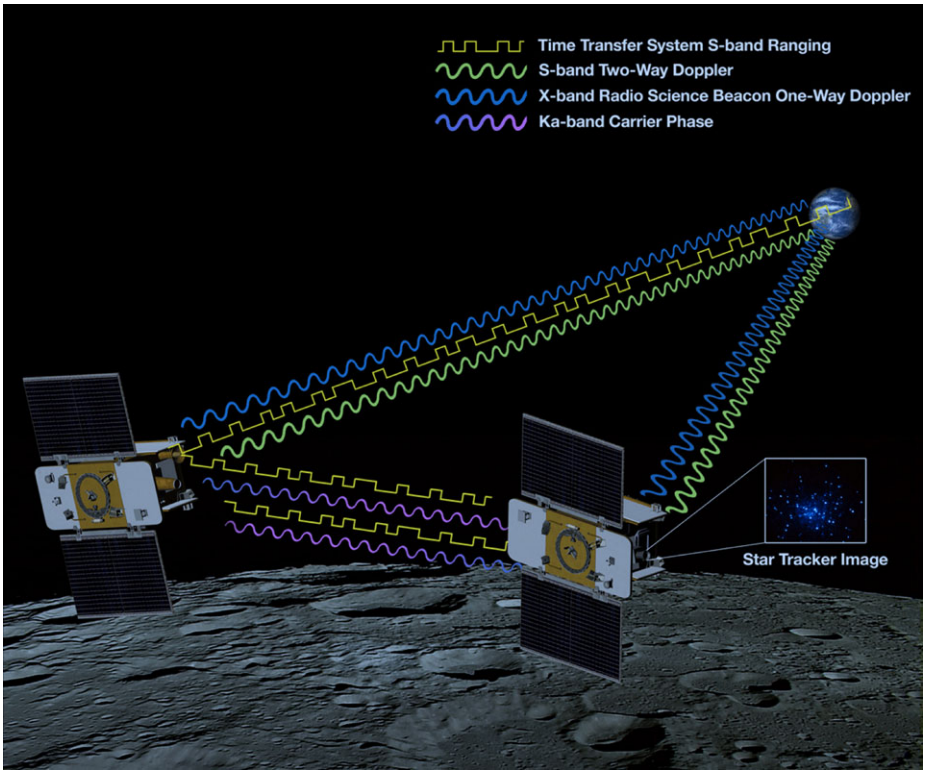

Fig. 1 The GRAIL radio links: Ka-band and S-band inter-spacecraft links, X-band one-way downlink to ground stations, and two-way S-band links for telecommunications and navigation

on one Ultra-Stable Oscillator (USO) per spacecraft. The navigation and telecommunications telemetry and command functions are handled by a separate two-way S-band link with the DSN. This is a spacecraft system function not linked to the science payload or the USO. The science data quality simulations did not incorporate the utility of this telecommunications link since no science performance requirements were imposed on it, but in reality, the science team collaborated with the navigation team to assess its usability to enhance the science results.

2 Simulations Tool and Data Levels

Over several decades, NASA's JPL has developed techniques, algorithms, and software tools to conduct investigations of planetary gravitational fields and applied them to practically every planet in the solar system and several satellites of the outer planets. JPL relies primarily on the Orbit Determination Program (ODP) whose formulation is detailed in Moyer (2003). The ODP has enabled precision navigation for the vast majority of deep space missions and, due to its criticality to the success of these missions, has received rigorous development and testing as well as continued improvements (a new tool called Mission-analysis, Operations, and Navigation Toolkit Environment, or MONTE, has replaced the ODP for mission navigation purposes).

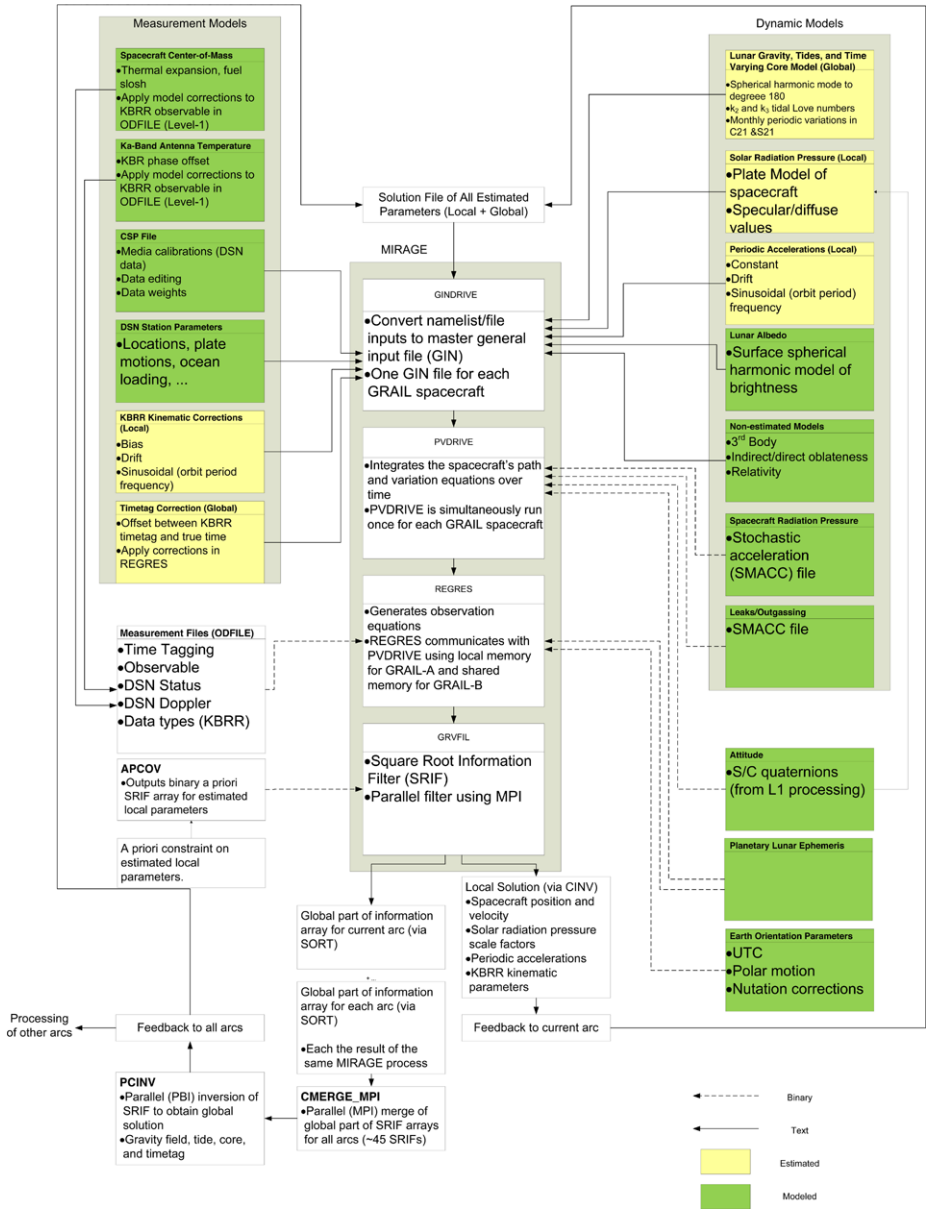

Fig. 2 A functional flowchart of the MIRAGE software tool as used in the simulation process

The GRAIL scientists at JPL use a version of the ODP called Multiple Interferometric Ranging and GPS Ensemble (MIRAGE), which originated from a GPS version of the ODP developed for the TOPEX mission (described in Guinn and Wolff 1993, and Leavitt and Salama 1993) and further developed for gravity field analysis, (Fahenstock 2009). Figure 2 shows the MIRAGE flowchart process utilized for GRAIL and the various programs that process the generalized inputs, the spacecraft path integration, computation of dynamic pa-

rameter partials, and the data observables. This figure documents the necessary interfaces between the software elements and input/output files as well as the relevant computational parameters and has been a key figure for the simulations peer-review process. There are three subsets of programs that integrate the spacecraft motion, process the spacecraft observations and filter or estimate the spacecraft state and related parameters using the observations.

To determine the spacecraft dynamical path, the program numerically integrates the spacecraft Cartesian state by including all known forces acting on the spacecraft, such as gravity, solar pressure, lunar albedo, and spacecraft thrusting. The spacecraft state and the force model partial derivatives (e.g., gravity harmonics) that are later estimated are integrated using the variable order Adams method described in Krogh (1973). The non-rotating International Celestial Reference Frame (ICRF) defines the inertial coordinate system, which is nearly equal to the Earth's mean equator and equinox at the epoch of J2000.

The GRAIL data are categorized in 3 levels, also shown in of Zuber et al. (2013, this issue). Level 0 is the raw data acquired by the spacecraft science payload, the LGRS, and DSN Doppler. Level 1 is the expanded, edited and calibrated data. Level 1 processing is the conversion from Level 0 files to Level 1 files. Level 1 processing also applies a time tag conversion, time of flight correction, and phase center offset, as well as generates instantaneous range-rate and range-acceleration observables by numerical differentiation of the biased range observables. Level 2 is the gravity field spherical harmonic expansion; level 2 processing refers to the production of Level 2 data. The simulations described herein emulate the generation of Levels 1 and 2 GRAIL mission data.

3 Gravity Model Representation

Gravitational fields provide a key tool for probing the interior structure of planets. The lunar gravity, when combined with topography, leads to geophysical models that address important phenomena such as the structure of the crust and lithosphere, the asymmetric lunar thermal evolution, subsurface structure of impact basins and the origin of mascons, and the temporal evolution of crustal brecciation and magmatism. Long-wavelength gravity measurements can place constraints on the presence of a lunar core.

A gravitational field represents variations in the gravitational potential of a planet and gravity anomalies at its surface. It can be mathematically represented via coefficients of a spherical harmonic expansion whose degree and order reflect the surface resolution. A field of degree 180, for example, represents a half-wavelength, or spatial block size, surface resolution of 30 km; for degree n, the resolution is $30 \times 180/n$ km. The gravitational potential in spherical harmonic form is represented in the body-fixed reference frame with normalized coefficients ($\overline{C}_{nm}$, $\overline{S}_{nm}$) is represented after Heiskanen and Moritz (1967) and Kaula (1966) as:

$$U = \frac{GM}{r} + \frac{GM}{r} \sum_{n=1}^{\infty} \sum_{m=0}^{n} \left(\frac{R_e}{r} \right)^n \overline{P}_{nm}(\sin \varphi_{lat}) \left[\overline{C}_{nm} \cos(m\lambda) + \overline{S}_{nm} \sin(m\lambda) \right] \quad (1)$$

G is the gravitational constant, M is the mass of the central body, r is the radial distance coordinate, m is the order, $\overline{P}_{nm}$ are the fully normalized associated Legendre polynomials, R_e is the reference radius of the body, φ_{lat} is the latitude, and λ is the longitude. The gravity coefficients are normalized so that the integral of the harmonic squared equals the area of a unit sphere, and are related to the un-normalized coefficients by Kaula (1966), where δ is

the Kronecker delta:

$$\begin{pmatrix} C_{nm} \\ S_{nm} \end{pmatrix} = \left[\frac{(n-m)!(2n+1)(2-\delta_{0m})}{(n+m)!} \right]^{1/2} \begin{pmatrix} \overline{C}_{nm} \\ \overline{S}_{nm} \end{pmatrix} = f_{nm} \begin{pmatrix} \overline{C}_{nm} \\ \overline{S}_{nm} \end{pmatrix} \tag{2}$$

There exist singularities at the pole in the partials of the gravity acceleration with respect to the spacecraft position when using the Legendre polynomials as a function of latitude. To accommodate this, MIRAGE uses a nonsingular formulation of the gravitational potential, including recursion relations given by Pines (1973), in calculation of the acceleration and partials.

The gravitational potential also accounts for tides caused by a perturbing body. The second-degree tidal potential acting on a satellite at position $\vec{r}$ relative to the central body, with the perturbing body (e.g., Sun and Earth for GRAIL) at position $\vec{r}_p$, is:

$$U = k_2 \frac{GM_p}{R} \frac{R^6}{r^3 r_p^3} \left[\frac{3}{2} (\hat{r} \cdot \hat{r}_p)^2 - \frac{1}{2} \right] \tag{3}$$

where k_2 is the second degree potential Love number, M_p is the mass of the perturbing body causing the tide, and R is the equatorial radius of the central body. Tides raised on the Moon by the Sun are two orders-of-magnitude smaller than tides raised by the Earth. The acceleration due to constant lunar tides is modeled using a spherical harmonics representation:

$$\Delta C_{nm} - i \Delta S_{nm} = \frac{k_{nm}}{2n+1} \sum_j \frac{GM_j}{GM} \frac{R_M^{n+1}}{r_{mj}^{n+1}} P_{nm}(\sin \varphi_j) e^{-im\lambda_j} \tag{4}$$

Simplifying, the non-dissipative tides contribute time-varying components to second degree and order normalized coefficients as follows (McCarthy and Petit 2003):

$$\begin{aligned}
\Delta \overline{J}_2 &= -k_{20} \sqrt{\frac{1}{5}} \frac{GM_p R^3}{GMr_p^3} \left[\frac{3}{2} \sin^2 \varphi_p - \frac{1}{2} \right] \\
\Delta \overline{C}_{21} &= k_{21} \sqrt{\frac{3}{5}} \frac{GM_p R^3}{GMr_p^3} \sin \varphi_p \cos \varphi_p \cos \lambda_p \\
\Delta \overline{S}_{21} &= k_{21} \sqrt{\frac{3}{5}} \frac{GM_p R^3}{GMr_p^3} \sin \varphi_p \cos \varphi_p \sin \lambda_p \\
\Delta \overline{C}_{22} &= k_{22} \sqrt{\frac{3}{20}} \frac{GM_p R^3}{GMr_p^3} \cos^2 \varphi_p \cos 2\lambda_p \\
\Delta \overline{S}_{22} &= k_{22} \sqrt{\frac{3}{30}} \frac{GM_p R^3}{GMr_p^3} \cos^2 \varphi_p \sin 2\lambda_p
\end{aligned} \tag{5}$$

Here, φ_p and λ_p are the latitude and longitude of the perturbing body on the surface of the central body. Separate Love numbers have been used for each order, though they are expected to be equal ($k_{20} = k_{21} = k_{22}$). Degree-3 Love number solutions have been investigated and their effect is barely detectable.

The tidal potential consists of a variable term and a constant or permanent term. Depending on choice of convention, the constant term may or may not be included in the corresponding gravity coefficient. The MIRAGE-generated gravity fields do not include the

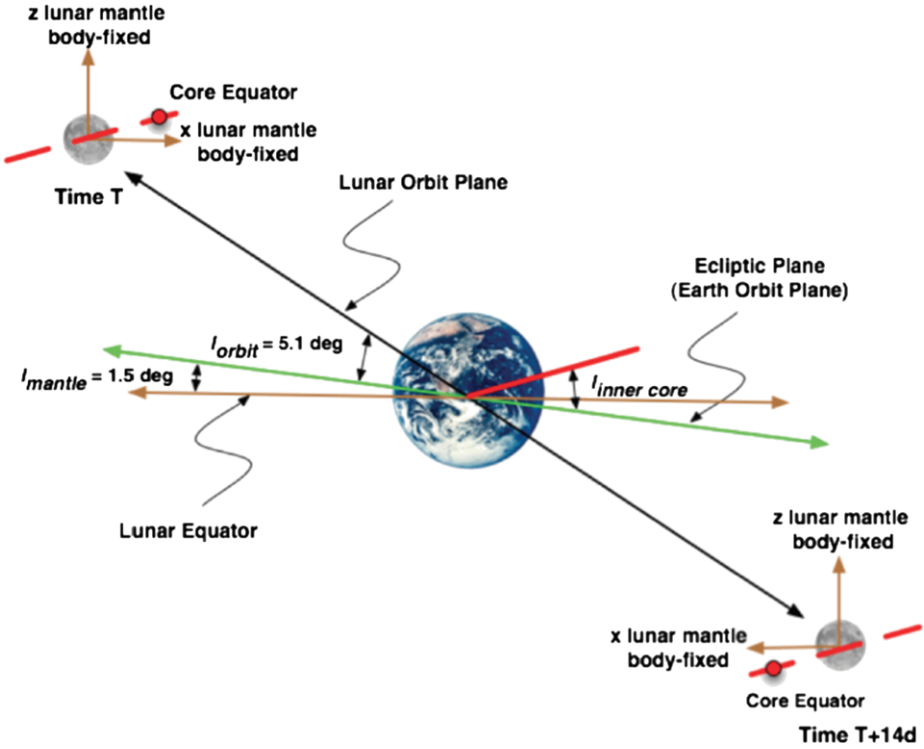

Fig. 3 Possible lunar core motion and the relationship between different frames of reference

permanent part of the tide. Our formulation assumes an elastic Moon and does not include the frequency-dependent dissipation terms. The elasticity does not affect the overall simulation results and was not considered in this study. The k_2 estimate uncertainty from lunar laser ranging and spacecraft tracking is between 6–8 percent. The GRAIL results will determine the k_2 Love number to better than 1 percent.

The acceleration due to the gravitational potential must be rotated from the body-fixed principal axis frame to the inertial frame using the lunar physical libration angles included in a planetary ephemeris database (e.g., JPL DE421) described in Williams et al. (2008). Three Euler angles describe lunar orientation: the angle along the J2000 equator from the J2000 equinox to the intersection of the lunar equator with the J2000 equator, the angle between the two equators, and the angle along the lunar equator from the intersection of equators to the lunar meridian of zero longitude (Newhall and Williams 1997).

On the basis of re-analysis of Apollo seismic observations, Weber et al. (2011) proposed that the Moon has a solid inner core surrounded by a fluid outer core. Given an oblate inner core, a time-varying signature could result from the monthly motion of the lunar core equator relative to the lunar body-fixed or mantle frame (Williams 2007), affecting the degree 2 and order 1 spherical harmonics and the second-degree tidal potential changes due to the Earth and Sun. Figure 3 illustrates the Moon's expected core motion; a point on the core equator moves relative to the body-fixed equator with a period of one month.

Due to the pole offset of the core and mantle frame, the core motion introduces a monthly signature in the $\overline{C}_{21}$ and $\overline{S}_{21}$ gravity coefficients as follows:

$$\Delta\overline{C}_{21} = \alpha_{21}\cos(\dot{\omega}t + \varphi), \tag{6}$$

$$\Delta\overline{S}_{21} = \beta_{21}\cos(\dot{\omega}t + \varphi) \tag{7}$$

where $\Delta\overline{C}_{21}, \Delta\overline{S}_{21}$ is the monthly gravitational potential oscillation due to a possible solid inner core with an axis of rotation tilted relative to the mantle's axis, included in all simulations, $\dot{\omega}$ is the frequency and φ is the phase of this periodic signature. For the latter, we assume a priori knowledge when estimating the amplitudes of the $\overline{C}_{21}$ and $\overline{S}_{21}$ signatures (α_{21} and β_{21}) along with the gravity field and tidal Love number. If the inner core had an equilibrium figure for tide and spin distortion, then the ratio of amplitudes for $\overline{C}_{21}$ and $\overline{S}_{21}$ signatures would be 4. While this ratio is not assumed, it has been used to set requirements for amplitude uncertainties. We investigated both the uncertainty of the core amplitudes and the differences of the estimated values with the a priori values. These estimated amplitudes plus the tidal Love numbers encapsulate the results of GRAIL's science investigations addressing the deep interior.

4 Model Estimation and Dynamical Integration

JPL's gravity field estimation process relies on two primary data types: a link between the spacecraft and Earth, which is a one-way X-band link, and an inter-spacecraft link called the Ka-band Range (KBR). The latter's first derivative, the Ka-band Range Rate (KBRR), precisely measures the relative movement of Ebb and Flow, which permits estimation of the lunar gravity field. The combined measurement of two sets of ranging data, one measured by Ebb and a second by Flow, is called the Dual One-Way Range (DOWR) measurement. Ebb and Flow are tracked from Earth by the DSN, which produces Doppler data used to determine the absolute position of each spacecraft:

$$z_d = \hat{\rho}_{se} \cdot \dot{\rho}_{se}, \tag{8}$$

$$z_s = \hat{\rho}_{ba} \cdot \dot{\rho}_{ba} \tag{9}$$

where ρ_{se} represents the vector from spacecraft to the DSN station and ρ_{ba} represents the vector from Ebb to Flow.

The estimation of the gravity field follows the same steps as the orbit determination process in navigation but involves many more parameters and methods that may constrain the gravity field and other model parameters to obtain the most realistic solution. Although the planetary gravity field solutions often require a Kaula power law constraint (Kaula 1966), the uniform and global coverage of the KBRR data does not require a constraint in our simulations except for solutions of high degree (i.e., degree ~270) where a small power-type constraint was applied.

Letting $\vec{r}$ and $\vec{v}$ be the position and velocity vectors of the spacecraft relative to the central body, the software integrates the second order differential equations

$$\ddot{\vec{r}} = \vec{f}(\vec{r}, \vec{v}, \vec{q}) = \nabla U(\vec{r}) + \vec{f}_{pm} + \vec{f}_{in\text{-}pm} + \vec{f}_{in\text{-}obl} + \vec{f}_{srp} + \vec{f}_{alb} + \vec{f}_{att} + \vec{f}_{rel} + \cdots \tag{10}$$

Here, $\vec{f}(\vec{r}, \vec{v}, \vec{q})$ is the total acceleration of the spacecraft and $\vec{q}$ are all the constant ($\dot{\vec{q}} = 0$) model parameters to be estimated (e.g., gravity harmonic coefficients). Contributions to the

total acceleration include the acceleration of the spacecraft relative to the central body due to the gravitational potential of the central body $\nabla U(\vec{r})$, the spacecraft acceleration due to other solar system bodies treated as point masses $\vec{f}_{pm}$, the indirect point mass acceleration of the central body in the solar system barycentric frame due to the other planets and natural satellites $\vec{f}_{in\text{-}pm}$, the indirect oblateness acceleration of the central body (e.g., Moon) due to another body's oblateness (e.g., Earth) $\vec{f}_{in\text{-}obl}$, the acceleration of the spacecraft due to solar radiation pressure $\vec{f}_{srp}$, the acceleration due to lunar albedo $\vec{f}_{alb}$, the acceleration due to spacecraft gas thrusting for attitude control maneuvers (usually for de-spinning angular momentum wheels) $\vec{f}_{att}$, and the pseudo-acceleration due to general relativity corrections $\vec{f}_{rel}$. Other accelerations also exist and may include spacecraft thermal forces, infrared radiation, tides, and empirical, usually periodic, acceleration models. Specific acceleration models that have been taken into account are described below.

4.1 Acceleration Due to Solar Radiation Pressure

Each spacecraft is modeled with five single-sided flat plates to model the acceleration due to solar radiation pressure (SRP) as detailed in Fahnestock et al. (2012) and Park et al. (2012). For each plate, the acceleration is computed as:

$$a_{srp} = \frac{CS_s}{m_s r_{sp}^2}(F_n \hat{u}_n + F_r \hat{u}_s), \tag{11}$$

$$F_n = -A(2\kappa_d v_d + 4\kappa_s v_s \cos\alpha)\cos\alpha, \tag{12}$$

$$F_r = -A(1 - 2\kappa_s v_s)\cos\alpha. \tag{13}$$

The acceleration due to SRP is on the order of 10^{-10} km/s^2. It is separable from the effect of gravity in the estimation process. With a ray-tracing technique to model self-shadowing on the spacecraft bus and on-board telemetry of the power system to detect entry and exit from lunar shadow, the SRP accelerations can be determined to a few percent level.

4.2 Acceleration Due to Spacecraft Thermal Radiation:

For a flat plate component, the acceleration due to spacecraft thermal re-radiation is:

$$a_{str} = \frac{-2 \times 10^{-6} A \sigma_{sb}}{3 m_s c} \varepsilon T^4 \hat{u}_n. \tag{14}$$

This is used to convert from any given plate's surface temperature to its acceleration contribution.

4.3 Acceleration Due to Lunar Albedo and Thermal Emission

The element of acceleration on a spacecraft due to lunar radiation pressure from a point P on the surface of the Moon can be computed (from Park et al. 2012) as:

$$da_{lrp} = H(F_n \hat{u}_n + F_r \hat{r}_{ps}) \frac{\cos\psi}{\pi r_{ps}^2} dA_{planet}. \tag{15}$$

For reflected sunlight (albedo):

$$H = \frac{CS_m \cos\psi_s}{m_s r_{ms}^2} \sum_{\ell=0}^{N} \sum_{m=0}^{\ell} \left(C_{\ell m}^A \cos m\lambda_p + S_{\ell m}^A \sin m\lambda_p\right) P_{\ell m}(\sin\varphi_p), \tag{16}$$

and for thermal emission (infrared):

$$H = \frac{C}{4m_s r_{ms}^2} \sum_{\ell=0}^{N} \sum_{m=0}^{\ell} \left(C_{\ell m}^E \cos m\lambda_p + S_{\ell m}^E \sin m\lambda_p\right) P_{\ell m}(\sin \varphi_p). \tag{17}$$

The albedo map is a constant field whereas the thermal map is a function of local lunar time because of topographic variation; the thermal map derived using the measurements from Lunar Reconnaissance Orbiter's Diviner Lunar Radiometer Experiment data. For this reason, the following simplified thermal emission model was derived for the simulation of the total error budget:

$$H = \begin{cases} \frac{C\sigma_{sb} T_{\max}^4 \cos \psi_s}{4m_s r_{cs}^2 L}, & \text{if } \psi_s \leq 89.5^\circ, \\ \frac{C\sigma_{sb} T_{\min}^4}{4m_s r_{cs}^2 L}, & \text{otherwise,} \end{cases} \tag{18}$$

where $T_{\max} = 382.86$ K and $T_{\min} = 95$ K. Thermal maps were computed at the local noon-time when the Sun is at 0° longitude and 0° latitude.

4.4 Acceleration Due to Un-modeled Forces

The acceleration due to un-modeled forces is used to represent the errors in the non-gravitational forces from solar pressure, spacecraft thermal radiation, lunar radiation, and spacecraft outgassing and is represented as the periodic acceleration formulation:

$$\begin{aligned} a_{uf} = {} & (P_r + C_{r1} \cos\theta + C_{r2} \cos 2\theta + S_{r1} \sin\theta + S_{r2} \sin 2\theta)\hat{e}_r \\ & + (P_t + C_{t1} \cos\theta + C_{t2} \cos 2\theta + S_{t1} \sin\theta + S_{t2} \sin 2\theta)\hat{e}_t \\ & + (P_n + C_{n1} \cos\theta + C_{n2} \cos 2\theta + S_{n1} \sin\theta + S_{n2} \sin 2\theta)\hat{e}_n, \end{aligned} \tag{19}$$

where $\hat{e}_r$, $\hat{e}_t$, and $\hat{e}_n$ represent the radial, transverse, and normal unit-vectors, respectively and θ denotes the angle from the ascending node of the spacecraft orbit on the EME2000 plane to the spacecraft. The periodic acceleration is nominally set to zero in the initial trajectory integration and is used to estimate the errors in the non-gravitational accelerations. The terms P_i represent the constant accelerations during the time interval that the corresponding periodic acceleration model is active. The terms (C_{i1}, S_{i1}) and (C_{i2}, S_{i2}) represent the once-per-orbit and twice-per-orbit acceleration amplitudes, respectively.

In addition to integrating the spacecraft position and velocity, MIRAGE integrates the variational equations to estimate the epoch state and constant parameters. Following nomenclature in Tapley et al. (2004a, 2004b), the nominal trajectory is given by:

$$X^*(t) = \begin{pmatrix} \vec{r}^*(t) \\ \vec{v}^*(t) \\ \vec{q}^* \end{pmatrix}. \tag{20}$$

The first order differential equation to integrate in order to determine the nominal orbit is:

$$\dot{X}^*(t) = \begin{pmatrix} \vec{v}^* \\ \vec{f}(\vec{r}^*, \vec{v}^*, \vec{q}^*) \\ 0 \end{pmatrix} = F\left(X^*, t\right). \tag{21}$$

The variation of the trajectory from its nominal path is $x(t) = X(t) - X^*(t)$ and the linearized equations:

$$\dot{x}(t) = A(t)x(t) = \left(\frac{\partial F(t)}{\partial X(t)}\right)^* x(t) \tag{22}$$

The integrated solution is the state transition matrix $\Phi(t, t_0)$, which relates the deviation from the nominal path at epoch t_0 to the deviation from the nominal path at time t for the 6 position and velocity epoch parameters matrix ($U_{6\times6}$) and the p constant model parameters ($V_{6\times6}$):

$$x(t) = \Phi(t, t_0)x(t_0) = \begin{bmatrix} U_{6\times6} & V_{6\times6} \\ 0_{p\times6} & I_{p\times p} \end{bmatrix} x(t_0). \tag{23}$$

The second order differential equations that MIRAGE integrates for each GRAIL spacecraft include the 3 position variables of Eq. (10), 18 variables representing the changes in position and velocity due to small changes in epoch position and velocity which define the matrix $U_{6\times6}$, and three equations for each dynamic parameter or constant from being estimated. For a complete gravity field of degree and order n, the total number of gravity field parameters is given by $(n-1)(n+3)$, or, for example, 32,757 parameters for a 180 degree and order field.

5 Processing and Filtering of Observations

After numerical integration, MIRAGE processes Doppler and range observations. Following Tapley et al. (2004a), the general form of the observation equation is

$$Y = G(X, t) + \varepsilon, \tag{24}$$

where Y is the actual observation, $G(X, t)$ is a mathematical expression to calculate the modeled observation value, and ε is the observation error. The DSN Doppler data is not an instantaneous velocity measurement, but is processed in similar fashion to a range observable and is given by a differenced range measurement for two-way Doppler as

$$G(X, t) = \big((r_{12} + r_{23})_e - (r_{12} + r_{23})_s\big)/\Delta t + \cdots \tag{25}$$

where r_{12} is the uplink range transmitted by the ground station and received at the spacecraft, and r_{23} is the downlink range from the spacecraft to the earth station, with subscripts denoting the end and start of the Doppler count interval, Δt. To process a Doppler observation, we must solve the light time equation in a solar system barycentric frame, i.e., find the original transmit time at the first station and the receive time at the spacecraft using an iterative procedure. Equation (25) requires DSN calibrations for Earth ionospheric and tropospheric refraction (Mannucci et al. 1998), and corrections for relativistic propagation delay due to the Sun and planets, solar plasma delays due to the solar corona of the Sun, and any measurement biases.

The dual one-way phase measurement between Ebb and Flow can be converted to a biased range, by an algorithm first developed by Kim (2000). Our lunar gravity recovery process ingests instantaneous range-rate, modeled as a projection of the velocity difference vector, $\dot{r}_{12}$, along the line-of-sight unit vector, $\widehat{e}_{12}$.

$$G(X, t) = \dot{\rho} = \dot{r}_{12} \bullet \widehat{e}_{12} \tag{26}$$

Processing observables also requires the linearized form of Eq. (24). Given an observable Y, we compute a nominal observable $Y^*(t)$ based on an input nominal orbit, and calculate an observation residual y:

$$y = Y - Y^*(t) \tag{27}$$

Using the state transition matrix to map to the epoch time, Eq. (24) is then written as

$$y = \left(\frac{\partial G}{\partial X}\right)\Phi(t, t_0)x_0 + \varepsilon = Hx_0 + \varepsilon. \tag{28}$$

Based on the vector of residuals y and partials matrix H, the MIRAGE filter solves for a state X that minimizes these ε error terms.

The calculation of the nominal DSN Doppler observable and related partials in Eq. (28) involves the precise location of the Earth station in a solar system barycentric ICRF frame as shown in Yuan et al. (2001). The Earth-fixed coordinate system is consistent with the International Earth Rotation and Reference Systems Service (IERS) terrestrial reference frame labeled ITRF93 as shown in Boucher et al. (1994). The rotation of the Earth-fixed coordinates of the DSN locations to the Earth centered inertial system requires a series of coordinate transformations due to precession as in the IAU 1976 model described in Lieske et al. (1977) and nutation of the mean pole as in the IAU 1980 nutation theory described in Wahr (1981) and Seidelmann (1982) plus daily corrections to the model from the JPL Earth Orientation Platform (EOP) product of Folkner et al. (1993), rotation of the Earth as in Aoki et al. (1982) and Aoki and Kinoshita (1983) and UTC-UT1R corrections of the JPL EOP file, and polar motion of the rotation axis. The JPL EOP product is derived from the Very Long Baseline Interferometry (VLBI) and Lunar Laser Ranging (LLR) observations and includes Earth rotation and polar motion calibrations and, in addition, nutation correction parameters necessary to determine inertial station locations to the level of a few centimeters.

The body-fixed ITRF93 DSN station locations have been determined with VLBI measurements and conventional and GPS surveying. The coordinate uncertainties are about 4 cm for DSN stations that have participated in regular VLBI experiments, and about 10 cm for other stations; Folkner (1996) also provides the antenna phase center offset vector for each DSN station. These DSN station locations are consistent with the NNR-NEWVAL1 plate motion model (Argus and Gordon 1991). The variations of DSN station coordinates caused by solid Earth tide, ocean tide loading, and rotational deformation due to polar motion are corrected according to the IERS standards for 1992 (McCarthy and Petit 2003).

Once the observation equations are found, MIRAGE estimates the spacecraft state and other parameters using a weighted Square Root Information Filter (SRIF), see Lawson and Hanson (1995). SRIF computation time dominates MIRAGE processing, and for the larger planetary gravity fields of the Moon we run on two Beowulf Linux clusters (a 28-node machine with 112 CPU cores and a 45-node machine with 360 CPU cores). In normal form, the least-squares solution is given by:

$$\hat{x} = \left(H^T W H + P_{ap}^{-1}\right)^{-1} H^T W y \tag{29}$$

W is the weight matrix for the observations and P_{ap} is the a priori covariance matrix of the parameters being estimated. In the MIRAGE SRIF filter, the solution equation is kept in the form:

$$R\hat{x} = z \tag{30}$$

R is the upper triangular square-root of the information array and R and z are related to the normal equations as:

$$R^T R = H^T W H + P_{ap}^{-1}, \tag{31}$$

$$z = \left(R^T\right)^{-1} H^T W y \tag{32}$$

and the covariance P of the solution (inverse of the information array) is given by:

$$P = R^{-1}\left(R^{-1}\right)^T \tag{33}$$

We separate observations for gravity field determination into disjoint time spans called data arcs. Two-day-long data arcs are typical. The parameters estimated in the arc-by-arc gravity solutions consist of arc-dependent local variables: spacecraft state, solar radiation pressure coefficients, etc., and global variables common to all data arcs: gravity coefficients, tide parameters, etc. Merging the global parameter portion of a sequence of data arc square root information arrays produces a solution equivalent to solving for a single set of global parameters plus independent arc-specific local parameters (Kaula 1966).

When solving for a large number of parameters, convergence is very sensitive to a priori values and uncertainties. If the spacecraft initial state is poorly known and a filter tries to solve for both the trajectory and a high-resolution gravity field at the same time, the iteration may never converge. In order to avoid this problem, the local parameters are first estimated, and once a solution is obtained, the global parameters are estimated.

For each spacecraft, the local parameters consist of the spacecraft initial state, the solar radiation pressure scale factor, two constant SRP scaling terms orthogonal to the spacecraft-to-Sun vector, fifteen periodic acceleration terms for every two hours, four inter-satellite range-rate measurement correction terms for every two hours, and constant Earth-based Doppler bias and drift rate. Local parameters are used to constrain non-gravitational effects and measurement biases and are chosen based on experience. The global parameters consist of three inter-satellite range-rate time-tag biases, degree 2 and 3 Love numbers, degree 2 and order 1 amplitudes of periodic tidal signature, Moon's mass (GM), and a 150×150 gravity field (approximately 23,000 parameters). The time-tag biases represent the offset between the DSN time and a KBRR time-tag derived from the spacecraft clock.

Due to the accumulation of spacecraft angular momentum, maneuvers for Angular Momentum Desaturations (AMD) take place periodically. AMD maneuvers disrupt the quiet environment for gravity measurement and break the arc of data to be processed. Since we expect maneuvers, and to avoid numerical noise limitations on trajectory integration, we postulate 2-day arcs in our simulations. As described in Park et al. (2012), for each 2-day arc, we first estimate and re-estimate local parameters for each arc until convergence. Having converged on local parameters, we then compute SRIF arrays containing both local and global parameters for each arc, combine, and estimate, re-compute, re-combine, re-estimate, repeating until convergence.

6 Modeling Parameters

The input parameters to the simulations of the GRAIL mission are discussed below, grouped in the categories of data noise, data coverage, data arcs, orbital parameters, dynamic errors, and kinematic errors. To show the types of issues the simulation team was addressing, Table 2 lists a summary of parameters relevant to the simulation results and our model confidence in each one.

Table 2 Confidence level in GRAIL parameters relevant to science simulations

Parameter	Assumption	Note	Confidence level
Orbit initial conditions	Orbit conditions and spacecraft alignment are favorable	Inclination and node differences between spacecraft match requirements (0.02°)	High
Instrument noise spectrum	Spectrum includes thermal noise and USO jitter	GRACE analysis and performance modified for GRAIL	High
DSN data amount and noise	Tracking coverage is sufficient and noise characterization valid, includes USO	8 hours per day per spacecraft. DSN noise of 0.05 mm/s at 10-s integration time	High
KBR data continuity	No hardware resets	Tested with 5-min gaps once per day; show no impact	High
Time tag offset between payload and DSN time	Known to 100 ms, stable to 100 micro-seconds over 2 days	Convergence confirmed in science simulation	Medium to high
Temperature of spacecraft and payload elements	Linear dependence on beta angle	Tested conservatively, small error contribution	High
Propellant leakage	Constant and small	Preliminary information from spacecraft team	Medium
Outgassing	Small after cruise	Data from previous spacecraft	High
Lunar surface radiation	From lunar mission experience	Published models	Medium
Fuel slosh	Very small	Use of a propellant tank diaphragm	High
Solar radiation pressure	Constant reflectivity properties per arc and un-modeled errors <2 %	Currently investigating variability over an arc	Medium to high
Lunar librations	Modeled with Lunar Laser Ranging data	Known to a few milliseconds of arc	High
Lunar core signature	Monthly periodic	Phase not known	Medium

6.1 Data Noise

GRAIL simulations tools create DSN Doppler and inter-spacecraft Ka-band range rate data and apply noise to both data types. The simulations do not include DSN range data since this data type does not significantly improve GRAIL orbital accuracy. Since data noise levels are non-Gaussian, the applied noise and data weights assigned during follow-up parameter estimation are not always identical.

As discussed earlier, only the X-band Doppler link was included for simulation purposes, not the communications and navigation two-way S-band link between the DSN and the GRAIL spacecraft. The shorter wavelength X-band is less susceptible to ionosphere and interplanetary plasma noise. Expressed in units of velocity, our studies assume 0.05 mm/s DSN one-way X-band link residual noise and data weight at an integration time of 10 s, when simulating Doppler data and when filtering simulated data. This assumption is slightly more conservative than the typical noise level of 0.03 mm/s at 10 s experienced with the Mars Global Surveyor X-band performance.

The non-Gaussian residual noise associated with the payload's KBRR is added to the simulated inter-spacecraft data as a function of frequency. The long wavelength noise for 5-s samples is 0.4 μm/s for long wavelengths and then transitions to 1.0 μm/s at the short wavelength. However, in the filter, a constant data weight of 1 μm/s white noise is applied.

6.2 Data Coverage and Data Arcs

As a baseline, we simulated 8 hours of DSN daily tracking data for each spacecraft, non-overlapping, for a total of 16 hours. This DSN coverage provides information on absolute orbit for Ebb or Flow and improves long wavelength gravity field solutions, including the lunar core parameters, but contributes minimally to the global and regional science requirements. The coverage of the KBRR data is assumed to be continuous. Obtaining 16 hours of DSN coverage per day, every day, for one mission is considered very challenging due to the loading on the DSN but the requirements were accepted since the prime mission duration is relatively short, on the order of 3 months.

Since successive momentum dumps occur typically two days apart, GRAIL simulations assume a two-day data arc length, starting from an epoch of 4 March 2012 (actual epoch varied). Longer arcs are typically desirable but the momentum dumps are their natural boundaries.

6.3 Orbital Parameters

During the 82-day Science Phase, the Moon rotates three times underneath the GRAIL orbit. The collection of gravity data over one complete rotation, 27.3 days, is called one mapping cycle. Ebb and Flow are in a common near-polar, near-circular orbit with a mean altitude of approximately 55 km during the prime mission. However, as described in Roncoli and Fujii (2010) the periapsis altitude ranges from approximately 16 km to 51 km above a reference lunar sphere. The Ebb-Flow separation distance is designed to slowly vary. For approximately the first half of the mission, they drift apart and their separation distance increases from ∼85 to ∼225 km and then, with only one small orbit trim maneuver, they drift towards each other and the distance decreases to ∼65 km near the end of the mission. The shorter separation distance is optimum for data exploring the local and regional spatial features while the segment around the maximum separation is optimum for the determination of the global studies such as the lunar core parameters, which are the Love number and the periodic signature of degree 2. The separation distances are designed to ensure that there is no degradation of the Ka-band signal due to multipath off the lunar surface and, according to Roncoli and Fujii (2010), a shorter spacecraft separation is required because of the lower spacecraft altitude.

The spacecraft separation contains a drift in order to reduce the resonance effects corresponding to the harmonic of the separation distance. Resonance effect degradation occurs at harmonic degrees of the form $N = 360/(D/30)$ where D is the spacecraft separation. This corresponds to degrees 54, 108, and 162 for a 200-km separation distance. For a 50-km separation, the resonance occurs much later, starting at degree 216.

The spacecraft inclination varies between approximately 88.4 and 89.85 degrees with a twice-per-month periodic signature. The average inclination, approximately 89.1 degrees, is offset from a perfectly polar orbit to improve the determination of low degree harmonic coefficients, but kept to a minimum to reduce the gap in data coverage at the poles.

The GRAIL science orbital phase is limited in part by a solar beta angle constraint of 49 degree imposed by the capability of the electrical power system; the spacecraft cannot generate sufficient power from the solar arrays for angles below this constraint. Figure 14 of Roncoli and Fujii (2010) illustrates the time history of the solar beta angle as well as the relationship between beta angle and the duration of solar eclipse during the science phase; eclipse durations are a maximum at the beginning and end and no solar eclipses when the solar beta angle is near 90 degrees near the middle. For the simulations the Sun-angle is

represented after Park et al. (2012) with the inclination computed with respect to the lunar pole vector, as:

$$\beta = 90^\circ - \cos^{-1}(\hat{e}_h \cdot \hat{r}_{sm}) \tag{34}$$

To separate the non-gravitational signature from gravitational effects, a β angle of 90° is optimal. The spacecraft enters terminator crossing at $\beta \sim 76^\circ$, and for β-angles less than this, modeling non-gravitational forces becomes more difficult, as the perturbations change rapidly due to partial shadowing of the orbit.

6.4 Dynamic Errors

The MIRAGE filter estimates both local parameters that are dependent for each data arc and global parameters that are common to all data arcs. The local dynamic parameters that are estimated include three dimensionless parameters for the solar pressure model of each spacecraft, a constant scale factor for the force along the sun-spacecraft direction with a nominal value of 1.0 and an a priori uncertainty of 0.10 or 10 % of the solar pressure force, and a scale factor for each off normal directions with a nominal value of 0.0 and an a priori uncertainty of 0.02 or 2 % of the overall solar pressure force. The solar pressure is modeled as a box-wing plate model with appropriate specular and diffuse coefficient values for each plate. Since both spacecraft are nearly identical, the solutions for the solar pressure scale factors are expected to be nearly equal. Several gravity solutions were also generated with strong a priori correlations between the two spacecraft solar pressure solutions to force them to be nearly equal. This constraint improved the core parameter uncertainties by about 30 % but had little effect on the global and regional gravity requirements. The baseline approach, however, is to treat the solar pressure solution of each spacecraft independently.

To account for un-modeled residual solar pressure errors, 15 periodic coefficients are estimated for each spacecraft for each arc with a priori amplitude equal to ∼2 % of the solar pressure force, or 3×10^{-12} km/s^2. The coefficients include constant, once per revolution and twice per revolution amplitudes for the radial, orbit normal, and along the velocity directions.

The lunar albedo model is not part of the baseline simulations results but albedo errors were independently investigated and found to be minimal. The albedo surface representation is given by the 10th degree spherical harmonic expansion of Floberhagen et al. (1999). The lunar surface thermal re-radiation is also investigated and is similar in size to albedo. Another non-gravitational force to be considered for GRAIL is the thermal radiation force as a result of heating on the spacecraft; this force is assumed to be small.

In the estimation of the gravity field, we assume a nominal gravity field and a truth gravity field. For the early simulation, the lunar gravity model derived from the Lunar Prospector mission to degree and order 150 and designated LP150Q in Konopliv et al. (2001) was used as both the nominal and truth models. Simulations since then have also used the smaller LP100J lunar gravity model to degree 100 as the nominal model to test convergence to the LP150Q truth model for different modeling assumptions.

The global dynamic parameters that are estimated include a gravity field to a given degree, the second-degree Love numbers, and the periodic amplitudes of C_{21} and S_{21} for core detection. In order to reduce computation time, the globally estimated gravity field was to degree 150 and extrapolated the results to degree 180. With current assumptions about data quality, it is expected that the gravity field will be recovered to higher than degree and order 300, which would make the Moon the body with the highest known gravity resolution in the universe.

6.5 Kinematic Errors

In addition to dynamic errors, which directly affect the spacecraft orbit because of a force, there are kinematic errors that affect the KBRR or DSN Doppler observables directly. Most of the kinematic corrections are estimated as local parameters that affect only that data arc. For every GRAIL orbit period of ∼2 hours, a KBRR bias, drift, and cosine and sine once per revolution amplitudes are estimated. For a 2-day arc this amounts to 48 parameters being estimated. No a priori constraint is applied to these parameters. For each arc, one DSN Doppler bias and one drift parameter are estimated to correct the USO frequency for the X-band one-way Doppler.

The very important kinematic error of timing offsets is addressed in a separate section below. Other kinematic errors are investigated by introducing noise or systematic trends in the KBRR residuals. The KBRR noise spectrum includes error contributions from the USO and spacecraft attitude jitter and the simulation account for them with a spectrum ranging from 0.4 μm/s at the long-wave-length to 1 μm/s at the short wavelength. Errors due to the offset of the phase center from the line connecting the center-of-mass from each spacecraft are minimized by actively pointing the spacecraft to align the phase centers. The changes in the temperature of the payload antenna and related hardware are modeled as a systematic trend in the observables. The current models we have investigated are sinusoidal once per orbit tones of 80 μm, a twice per orbit tone, and a triangular shaped twice per orbit signature. Amplitudes of all of these depend on the Sun angle. There is also a small error due to a shift reactive to the Ka-band system. These errors have a small effect on the core parameters and a negligible effect on the global and regional requirements. Errors due to sloshing of the fuel in the spacecraft fuel tank are expected to be negligible.

7 Modeling System Contributions

GRAIL utilized an integrated scientific measurement system comprised of flight, ground, mission, and data system elements in order to meet the end-to-end performance required for achieving the scientific objectives. Simulations leading to end-to-end error budgets were used to optimize the design, implementation, and testing of these elements. Because the inter-spacecraft range and range-rate observables and the range-rate between each spacecraft and ground stations can be affected by the performance of all elements of the mission, they were all treated as parts of an extended science instrument or a science system.

7.1 Flight System

The flight system is the spacecraft, which is comprised of the orbiters and science payload. The orbiter is comprised of the spacecraft bus, heritage from the Experimental Satellite System 11 (XSS-11) mission, and subsystems described in Hoffman (2009). At the heart of the flight system is the LGRS payload. Its design and performance are detailed in Klipstein et al. (2013, this issue). Key components of the GRAIL payload, such as the USO and RSB, are discussed here in the context of the quality of radio links, Doppler data, timing effects, and end-to-end error budgets.

As discussed above, to assess the ability of the flight system to meet the science requirements, all known sources of dynamic and kinematic error were assessed for their possible contributions to the uncertainty of simulated solutions for the gravity field and time varying tidal and core parameters. Fahnestock et al. (2012) described how early calculations

of these effects revealed that the acceleration in reaction to spacecraft thermal re-radiation was among the dominating sources of solution uncertainty. Thus detailed modeling of the spacecraft's geometry, surface material, optical properties and thermal state was investigated along with approaches to the interface of such modeling with the science data processing.

First, a model of each spacecraft was constructed with plate surfaces defined for each spacecraft to cover the external area, not accounting for protuberances such as the thrusters and cameras. The two spacecraft are virtually identical but externally mirrored about the body-frame X–Z plane (see Fig. 4). Thermal modeling was performed by Lockheed Martin using the Thermal Desktop software, and for each spacecraft for the thermal loading conditions of varying beta angles. This included incident sunlight, lunar albedo and infra-red (IR) emission, and equipment power modes during the data acquisition period. Steady-state nodal temperature output, repeatable from orbit to orbit, was averaged over the plate surfaces to produce averaged temperature profiles for each plate surface over one orbit. These were used with the best available material optical properties, most measured after thermal vacuum bake-out, to compute body frame acceleration profiles over one orbit. These were then double interpolated over phase angle to obtain body frame acceleration at any epoch in the science mission.

As detailed in Fahnestock et al. (2012), the sensitivities of the thermal re-radiation acceleration history model with respect to assumptions and inputs were examined for impact on science. These included quantifying the difference spatial averaging of nodal temperature output versus no spatial averaging over the solar array surfaces, the sensitivity to extracting power from the solar arrays, the sensitivity to 3σ variations in the optical properties of every type of used material, and sensitivity to additive worst-case temperature biases on all surfaces.

A 5 K global bias bounded most changes resulting from realistic input variations. The difference in predicted thermal re-radiation acceleration history between that case and the nominal case was taken as indicative of the magnitude of un-modeled accelerations that would act on the spacecraft, which was used to create an a priori error model for the constant, and once and twice per orbit sinusoidal, periodic acceleration parameters in the simulations.

For the gravity field solution, the modeled thermal re-radiation acceleration history, a telemetry-derived thermal re-radiation acceleration history, or a hybrid of the two was included in the nominal dynamical model. For the first, the solar array bus open circuit voltage and short circuit current telemetry channels were utilized to determine the actual epoch of transit into and out of the Moon's shadow, and then the modeled history was shifted and stretched in time to match these transit times. For the telemetry-derived history, given n surfaces in the spacecraft model, each of $m < n$ instantaneous surface temperatures was set equal to the average of instantaneous readings of one or more temperature sensors, selected based on geometric proximity to that surface. Each of the $n - m$ remaining surface temperatures was set equal to the closest associated one of the m surface temperatures, plus a bias computed as the time average, over one orbit at $\beta = 90^\circ$ epoch, of the difference of the pre-flight thermal modeling output for the two surfaces in question. The $\beta = 90^\circ$ epoch had no eclipsing and was when the spacecraft were the most thermally and dynamically quiet, so we chose to tailor our mapping from sensor temperatures to surface temperatures to this time period. The hybrid history, illustrated in Fig. 5, was a combination of the modeled history for the Y and Z body axes directions, and the telemetry-derived history for body X axis direction. The apparent best methodology to use in data processing appears to be the hybrid thermal re-radiation acceleration history and a priori error model derived from it, as described earlier.

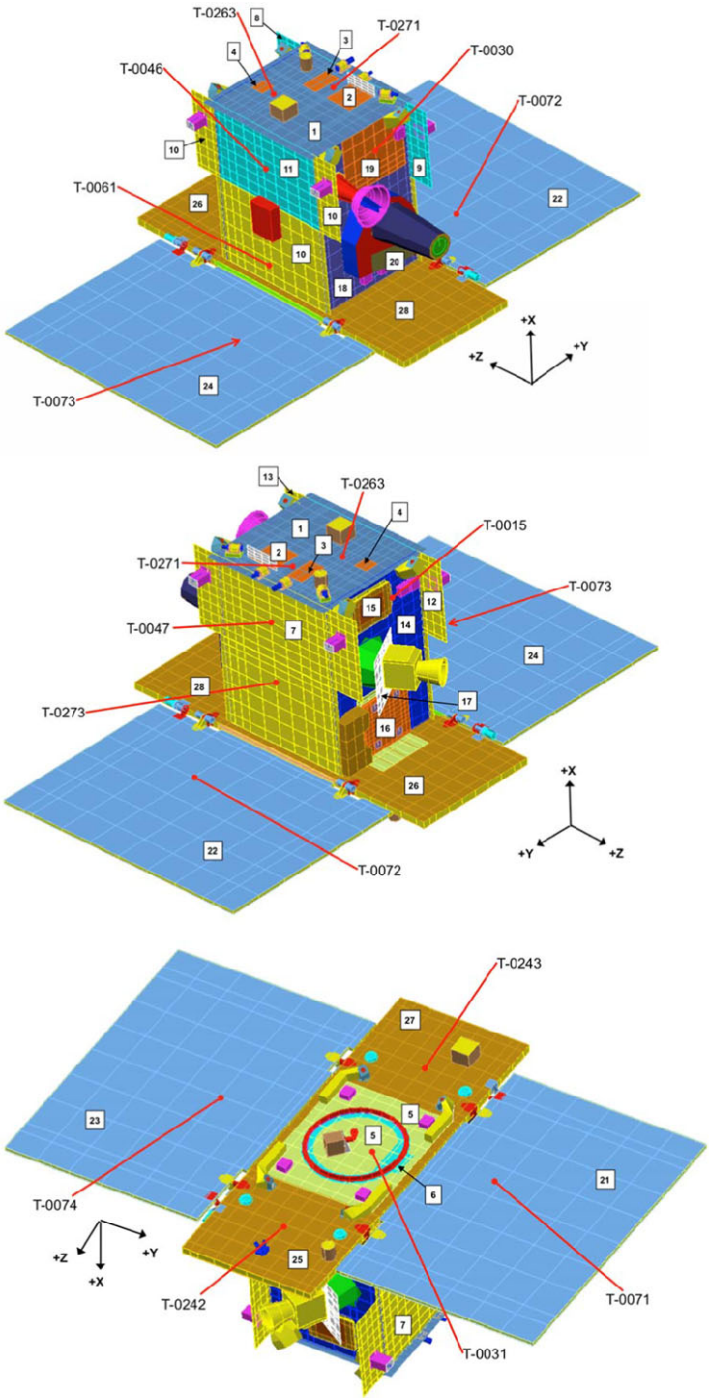

Fig. 4 Three views illustrating the placement of surfaces (*numbered in boxes*) on Flow's highest fidelity thermo-optical model, used for thermal re-radiation acceleration calculation. Ebb is similar, and temperature sensor locations are also noted

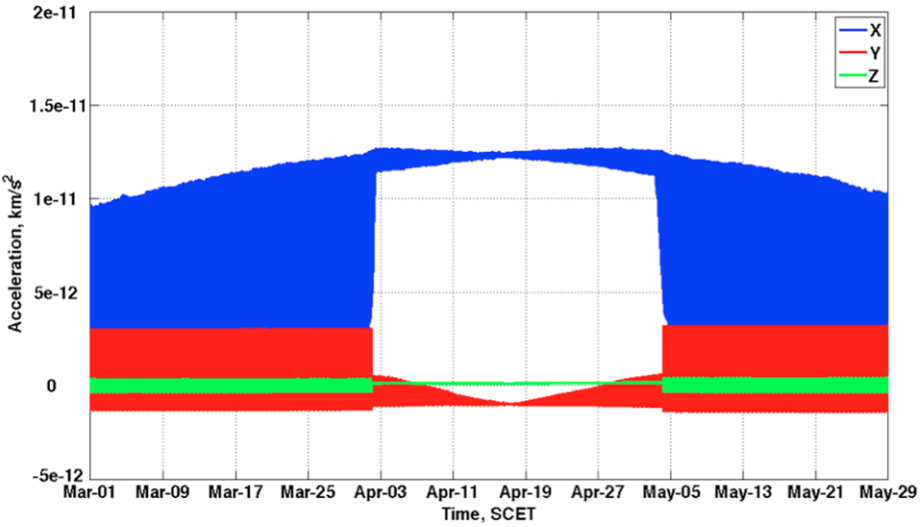

Fig. 5 Spacecraft body-frame components of hybrid thermal re-radiation acceleration history

The SRP acceleration was also included in the dynamical modeling in MIRAGE along with lunar albedo and IR emission pressure accelerations. For computing all three, a five-plate model of each spacecraft was obtained from the highest resolution model. This was done through combination of surfaces, first for common material and orientation, then for only common orientation, but always in a manner that kept the models roughly equivalent in four quantities: power coming into the spacecraft, acceleration due to SRP, power coming out of the spacecraft, and acceleration due to thermal re-radiation. All modeling of the non-gravitational accelerations within the spacecraft dynamics was sufficiently accurate to improve the orbit determination and data calibration as well as the gravity field solution.

7.2 Ground System

The ground system is comprised of the stations of the DSN, which was used exclusively by GRAIL, and the infrastructure facilities at JPL that support the DSN operations and transfer of data to users. The DSN's primary service to GRAIL and other missions is the telecommunications aspect, telemetry and commanding as well as navigation radio-metric data types. DSN services relevant to science are those providing precision measurements of the signal carrier frequency/phase for the purpose of Doppler observables. Two DSN subsystems Tracking and Radio Science are examined. As described earlier, GRAIL utilizes two bands for links to the DSN, a two-way S-band for telemetry, command, and navigation and a one-way X-band un-modulated carrier from the payload's RSB for science. As a result, DSN stations capable of S-band uplink and downlink as well as X-band downlink are required to support the mission, a criterion that narrows the available stations to a few 34-m diameter stations throughout the network but still enables the mission to get required coverage.

The Tracking Subsystem The Doppler data observable is generated in real-time at the DSN stations. The tracking receiver is a closed-loop system that finds the carrier frequency via a built-in algorithm and tracks it, aided by a prediction file for initial acquisition, producing the receiver's one-time real-time computation of the frequency and Automatic Gain Control

(AGC). Within its design threshold for dynamic conditions and signal-to-noise ratio, the output of the receiver is useful with a quantifiable Doppler noise that ranges between 0.02 and 0.1 mm/s. For GRAIL simulations, the X-band, USO driven link is associated with Doppler noise of 0.05 mm/s. If the threshold is exceeded, the receiver loses lock and data are not recoverable.

Radio Science Receiver Designed specifically for Radio Science experiments described in an overview by Asmar (2010), the DSN's Radio Science Receiver (RSR) is at the heart of an open-loop reception/recoding subsystem that preserves the raw qualities of the electromagnetic wave propagating from the spacecraft source to the DSN stations. The digital receiver neither locks onto the carrier signal nor makes real-time decisions about its frequency or amplitude. Instead, it down-converts the signal in a predictions-driven heterodyne method and records the raw complex samples into files for users' post-pass processing. Asmar et al. (2005) describes the RSR usage and typical performance derived from other missions.

The use of the RSR proved to be critical for enhancing the quantity and quality of GRAIL X-band Doppler data in two ways: (1) practically double the amount of RSB data received by the DSN by an unofficial use of the concept of multiple-spacecraft per aperture, where the DSN station scheduled to track Ebb, for example, also views Flow and vice versa, and (2) contribute to understanding the various timing effects, as explained at length in Sect. 8. GRAIL funded the development of 3 portable RSRs for use throughout the DSN in support of GRAIL data acquisition and timing synchronization.

7.3 Mission System

The mission operations system is comprised of the JPL and DSN infrastructure as well as the Lockheed Martin operations. Since the mission design affects science data quality, the following factors had to be very carefully considered: spacecraft altitude and spatial variation of the altitude, spacecraft separation distance, orbit inclination, ground track separation, mission duration, number of maneuvers, time separation of maneuvers, AMD separation, and amount of ground station coverage. Mission design, navigation, deep space stations, and the ground data system critically contribute to the quality of science data. Specifics of each factor were described above and additional details on the mission system can be found in Roncoli and Fujii (2010), Hatch et al. (2010), Beerer and Havens (2012), and Zuber et al. (2013, this issue).

7.4 Data System

The GRAIL Science Data System (SDS) is comprised of all project hardware and software tools that contribute to the quality of the science data. Sine the SDS team is the first team to assess the quality of the data on a daily basis, it provides immediate feedback to the Mission System on the health of the spacecraft, payload, or ground system in case action is required to address an anomaly.

Zuber et al. (2013, this issue) provides a functional block diagram of the SDS that shows the data flow from all the sources to the final science users and the archives of the Planetary Data System. For science data processing, delivery, and archiving, the SDS is organized to provide daily support including weekends in order to handle the data volume as well as prevent any oversight of anomalies for any extended period of time.

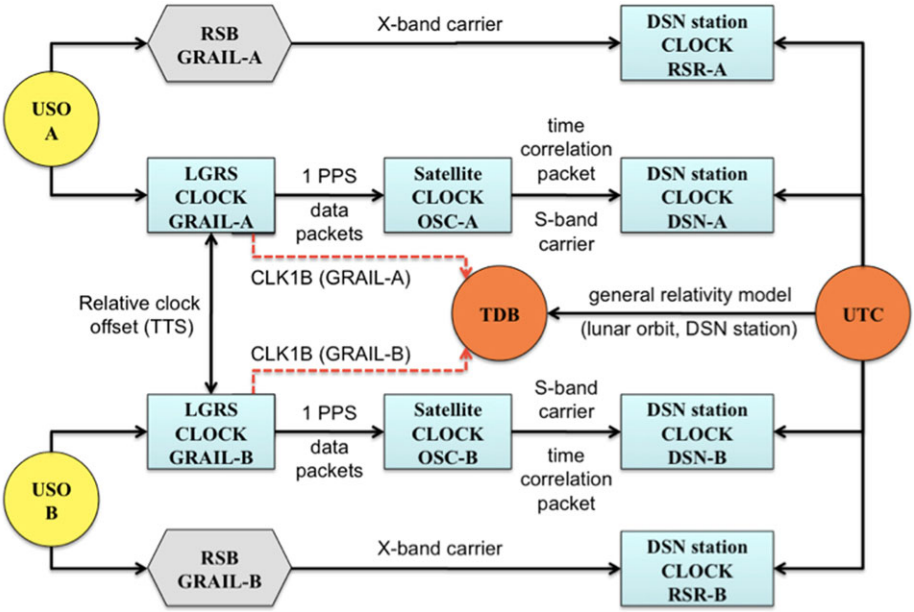

Fig. 6 Timing effects in the science data system

8 Data Timing and Synchronization

We have described how the process of determining the lunar gravity field starts with the inter-spacecraft Ka-band phase measurements used to compute the DOWR observables that are in turn converted to instantaneous range, range rate and range acceleration measurements. Very accurate timing of the measurements is crucial to achieve the high accuracy gravity results. The timing of the measurement has two components: absolute timing knowledge allows us to assign a measurement to a position around the Moon, and the relative timing knowledge between the payload clocks needed for the proper alignment of the LGRS phase measurements of both spacecraft at a common coordinate time. Following the formulation used in Kim (2000) and Thomas (1999), our analysis shows the aggregate errors in range to be below 1 μm and in range-rate to below 1 μm/s.

The GRAIL data are time-stamped on each spacecraft by the payload with time derived from the payload clock, namely the USO; Ebb and Flow each carries one USO that drifts independently from the other. The data are then passed to the spacecraft's central computer for packetizing prior to transmission to Earth as telemetry, and the computer puts a time-stamp on the packets derived from the spacecraft clock, which is independent from the USO. Finally, the data packets are received by the DSN and time-stamped at arrival, one-way light time after transmission, with the DSN time, which is derived from yet another independent clock. Counting two USOs, there are four independent clocks to synchronize in the post-processing in order to prevent errors in the gravity field solution, and this is carried out by the SDS team in the Level 1 processing stage as outlined in Fig. 6. The SDS team estimates the necessary time tag correction by combining information from available sources: the telemetry packets received at the DSN, the absolute frequency observed at the RSR, and the synchronization from the onboard inter-spacecraft TTS (note that additional observations were obtained at the DSN' RSR after launch of the inter-spacecraft TTS signals

edge to deduce the absolute time on-board and correlate it to the known USO drift resulting in micro-second level of accuracy, orders of magnitude better than time correlation packet information).

For the purpose of the simulations, it is assumed that the a priori clock offset knowledge is 100 milliseconds, constant over one month, and that the reconstruction of the time tag offset is ∼20 microseconds. To achieve such accuracies, the RSB was added to the science payload to transmit a one-way X-band un-modulated sine-wave signal generated by the USO and recorded by the DSN's RSR. The RSR measurement of the frequency bias is $<10^{-5}$ Hz and standard deviation $= 10^{-3}$ Hz.

The DSN clocks are synchronized with the highly stable Coordinated Universal Time (UTC) standard. GRAIL's data processing, on the other hand, utilizes Barycentric Dynamical Time (TDB). The timing analysis derives a time correlation between the LGRS clocks and the TDB time scale, to be provided as a Level 1 ancillary data product called CLK1B. To produce CLK1B relating LGRS and TDB, we preprocess the timing data types and run them through a non-causal Kalman filter.

The LGRS clock on each spacecraft is driven by the USO for maximum stability, which is 3×10^{-13} over integration times of 1 to 100 seconds, expressed in Allan Deviation. This clock, however, does not report the absolute time but reports readout with respect to the clock startup epoch with errors from the drift of the USO. Relying on the nearly quadratic behavior of the onboard clock and an assessment of relativistic contributions, we believe that this system enables determining the relative time on Ebb vs. Flow with a bias $< 10^{-7}$ s and standard deviation $= 9 \times 10^{-11}$ s.

The Onboard Spacecraft Clock (OSC) is derived from a crystal oscillator with inferior stability to the USO. The onboard computer tags LGRS timing data packets with OSC time, including the LGRS 1 Pulse Per Second (PPS) packet. Ebb and Flow transmit time correlation packets to DSN stations where the arrival time is recorded in UTC, which provides a time correlation between the OSC and UTC. The DSN uses very stable hydrogen maser clocks and time-stamps the arrival of telemetry and tracking data in the UTC frame, which is tied to the International Atomic Time (TAI) frame. Based on DSN monitoring reports, the real-time timing performance of DSN time-tags is at the microsecond level and post-processing analysis improves the performance to the 10^{-9} second level.

By combining the LGRS/OSC and OSC/UTC time correlation products, a time correlation between LGRS time and UTC can be determined and the OSC clock drops out. Because OSC error is under one microsecond over intervals shorter than one second, the stability characteristics of the OSC do not limit LGRS and UTC correlation accuracy. Considering possible unknown timing delays in packet transmission, we expect a measurement bias of up to 100 milliseconds, and standard deviation of up to 30 milliseconds.

9 Relativistic Effects

Turyshev et al. (2013) has developed a realization of astronomical relativistic reference frames in the solar system and its application to the GRAIL mission. A model was developed for the necessary space-time coordinate transformations for light time computations addressed practical aspects of the implementation and all relevant relativistic coordinate transformations needed to describe the motion of the GRAIL spacecraft and to compute observable quantities. Relativistic effects contributing to the double one-way range observable, which is derived from one-way signal travel times between the two GRAIL spacecraft were accounted for and a general relativistic model for this fundamental observable of GRAIL,

accurate to 1 μm and range-rate to 1 μm/s were also developed. The formulation justifies the basic assumptions behind the design of the GRAIL mission and may also be used in post-processing to further improve the results after the mission is complete.

It was recognized early during GRAIL's development phase that due to the expected high accuracy of ranging data, models of its observables must be formulated within the framework of Einstein's general theory of relativity in order to avoid significant model discrepancy. The ultimate observable model must correctly describe all the timing events occurring during the science operations of the mission for the links to Earth as well as the inter-spacecraft links. The model must take into account the different times at which the events have to be computed, involving the time of transmission of the Ka-band signal at one of the spacecraft, say Ebb, at the reception of this signal by its twin, Flow. In addition, the model must include a description of the process of transmitting S-band and X-band signals from both spacecraft and reception of this signal at a DSN tracking station.

Relevant points regarding relativistic corrections at the level of accuracy required by GRAIL include: (1) for a spacecraft around the Moon, we can model proper time treating the Moon as a point mass; (2) JPL's long-standing ODP models designed for proper time of a station on Earth are already sufficiently accurate, with no changes required; (3) up to a constant bias, computing one-way range from DOWR requires a pair of corrections from one-way light time to instantaneous distance. It suffices to iteratively solve for light time in terms of instantaneous distance, by re-computing transmission position bearing in mind the elapsed light time, in the presence of the Shapiro delay.

Turyshev et al. (2013) also notes that measuring the signal frequency involves computing three numbers: the derivative of proper time at the receiver with respect to coordinate time of reception, the derivative of proper time at the transmitter with respect to coordinate time of transmission, and the derivative of coordinate time of reception with respect to coordinate time of transmission. The first number must be modified to account for the fact that the clock at the DSN receiver attempts to synchronize with UTC time, rather than simply acting as a TDB receiver placed on the surface of the earth. The effect of the Earth's and the Moon's gravity on the third term will be below our level of error; if we did choose to include them it would certainly suffice to use a point mass.

10 Results of Simulations

10.1 A Priori Assumptions and Kaula Constraints

The a priori uncertainties for the models used in the simulations are summarized in Table 3. Furthermore, we assume that the KBRR data have $\sigma_s = 1$ μm/s uncertainty at 5-second count time, and the DSN Doppler tracking uncertainty at 10-second count time $\sigma_d = 0.05$ mm/s, obtained from previous payload and flight experience. The KBRR data give an average accuracy of 2×10^{-10} km/s^2, which is equivalent to 0.002 mGal in the gravity measurement.

Gravity field estimates often require a constraint by the Kaula rule (Kaula 1966). In this study, we assume the Kaula constraint to be $2.5 \times 10^{-4}/n^2$. Note that the Kaula constraint approximates the root-mean-square (RMS) of the spherical harmonics coefficients, i.e.,

$$\mathrm{RMS}_n = \sqrt{\frac{\overline{\sigma}_n^2}{2n+1}}, \tag{35}$$

for the degree variance $\overline{\sigma}_n^2 = \sum_{m=0}^{n} (\overline{C}_{nm}^2 + \overline{S}_{nm}^2)$.

Table 3 GRAIL simulations a priori uncertainty model

Parameters	A priori uncertainty
Position	1000 km in each direction
Velocity	1 m/s in each direction
Overall SRP scaling factor	10 %
Orthogonal SRP scaling factors	2 % in each direction
Doppler correction terms	open
LGRS correction terms	open
Periodic acceleration	Variable
Lunar gravity field	LP150Q solution
k_2, α_{21}, and β_{21}	open

Table 4 Baseline core-signature estimates

	$\Delta_{k2} \times 10^4$	$\sigma_{k2} \times 10^4$	$\Delta_{\alpha 21} \times 10^{10}$	$\sigma_{\alpha 21} \times 10^{10}$	$\Delta_{\beta 21} \times 10^{11}$	$\sigma_{\beta 21} \times 10^{11}$
Requirement		2.00		1.00		2.50
Baseline	0.93	0.94	0.62	0.67	−2.01	1.77

10.2 Dynamic Conditions and Core Signature Model Results

Table 4 shows the estimates of the core signature terms for the baseline case, where Δ_i represents the difference between the truth and the estimated parameter i and σ_i represents the estimated 1-σ uncertainty of parameter i. The effect of different data arc lengths, which are bounded by spacecraft maneuvers with a baseline of 2 days, is that the longer the arc the better the results for the core signature, as expected (Park et al. 2012). The baseline assumes Ebb and Flow are tracked by the DSN for at least 8 hours per spacecraft per day. Longer tracking is better and the diversified coverage over different DSN complexes provides additional orbit information due to geometric parallax.

The remaining possible error contributions from un-modeled non-gravitational accelerations are applied as an a priori periodic acceleration model that impacts the formal uncertainties of the estimated low-degree gravity field and time-varying core signature. The minimum periodic acceleration is chosen to be 3×10^{-13} km/s^2, as shown in Fig. 7, and scaled up accordingly for the period of lower spacecraft separation; with this minimum a priori periodic acceleration, all science requirements are met. We showed in Park et al. (2012) that varying the a priori periodic acceleration to the level of 1×10^{-12} km/s^2 still allows satisfying all science requirements but with smaller error margin for the core parameters.

10.3 Kinematic Error Results

Table 5 shows the effect of kinematics errors on the estimated core parameters. The error in the estimated parameters represents the effect due to kinematic errors and the formal uncertainties are the same as in the baseline case. The temperature control case shows the effect of the error in the LGRS measurement frequency and signal path-length due to thermal variation. The time-tag error shows the contribution to the total error of estimating the KBRR time tag with an initial time-tag offset of 100 milliseconds. Lastly, the attitude pointing error shows the effect of a 3-σ single-spacecraft attitude pointing error, which translates to about 0.06 μm/s on LGRS data.

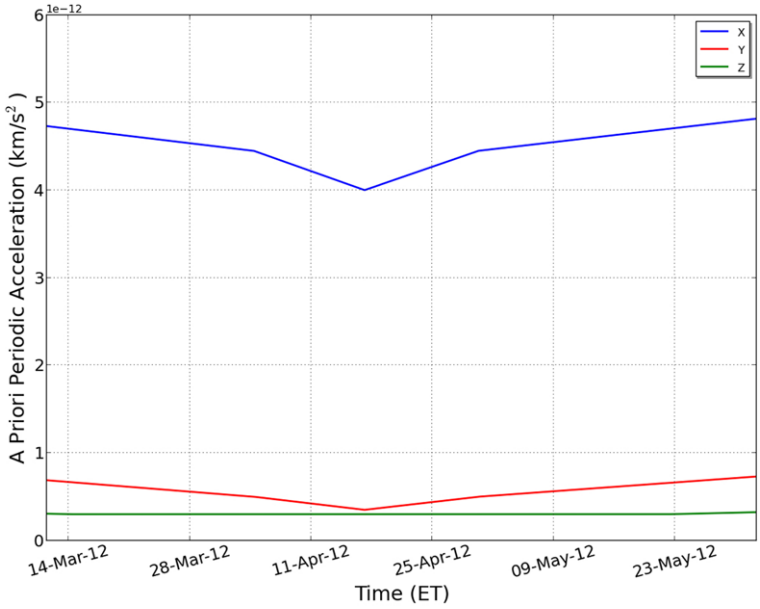

(A)

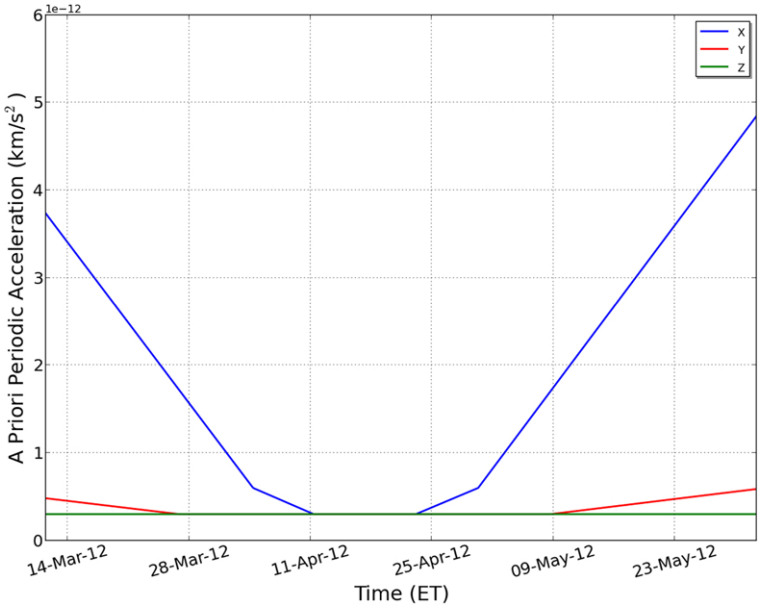

(B)

Fig. 7 A priori periodic acceleration with 3×10^{-13} km/s^2 minimum acceleration constant term in panel (**A**) and once-per-orbit and twice-per-orbit terms in panel (**B**) (Park et al. 2012)

Table 5 Effect of kinematics errors on estimated core parameters

Cases	$\Delta_{k2} \times 10^4$	$\Delta_{\alpha 21} \times 10^{10}$
Temperature control	0.05	0.01
Time-tag error	0.02	0.02
Attitude pointing error	0.20	0.10

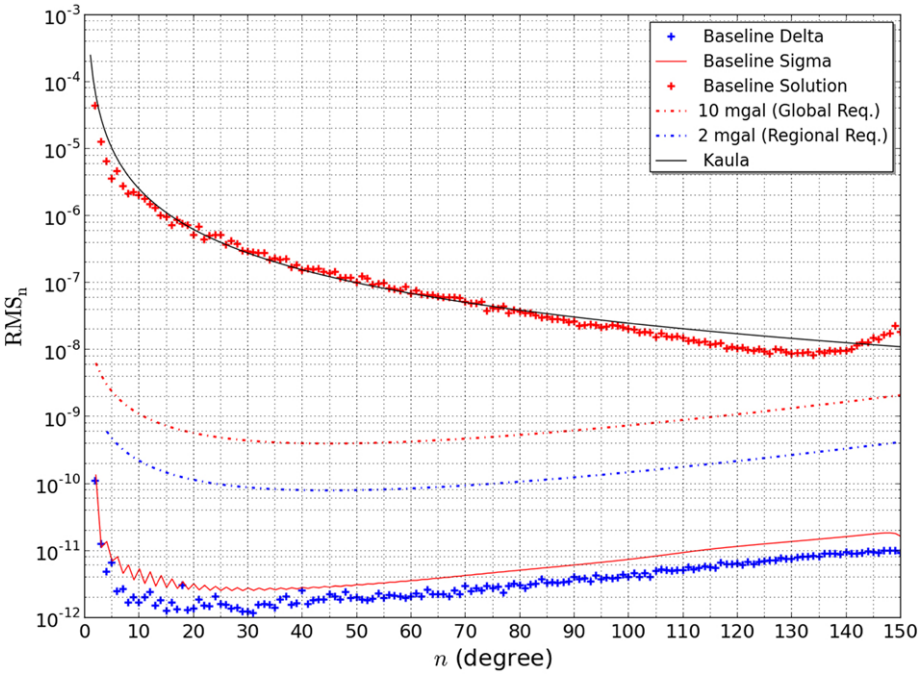

Fig. 8 Root mean square of the baseline simulation results

10.4 Summary

The most significant result of the simulations is the RMS of the estimated gravity field corresponding 1-σ formal uncertainties and the difference between the truth and estimated gravity fields, shown in Fig. 8. Also shown in the same figure are the global and regional science requirement lines generated based on the surface acceleration accuracy required for global and regional science requirements, which are satisfied with the baseline assumptions. The difference between the truth and estimated gravity fields is smooth and is bounded by the formal uncertainty indicating a correct filter setup and a stable filter solution. The colored measurement noise is well bounded by the white noise assumption that was used in the estimation process since the recovered values are well represented by the formal uncertainties. The linear extrapolation of the estimated uncertainties indicates that a nominal gravity field of degree 300 or better can be determined according to the Kaula rule. The largest source of non-gravitational error comes from spacecraft thermal radiation, which is characterized with variable a priori error constraint model derived from orbit geometry and expected force magnitude.

With all error models included, detailed and numerous simulations show that estimating the lunar gravity field is robust against dynamic and kinematic errors and meets the high accuracy lunar gravity requirements by at least an order of magnitude. A nominal lunar gravity field of degree 300 or better can be achieved according to the scaled Kaula rule for the Moon. The core signature is more sensitive to modeling errors and depends on how accurately the spacecraft dynamics can be modeled; the requirement can be achieved with a small margin.

Acknowledgements The GRAIL mission is supported by the NASA Discovery Program under contracts to the Massachusetts Institute of Technology and the Jet Propulsion Laboratory. The work described in this paper was mostly carried out at Jet Propulsion Laboratory, California Institute of Technology, under contract with the National Aeronautics and Space Administration. The authors thank colleagues who have contributed to this work or reviewed it, especially at JPL: Duncan McPherson, Ralph Roncoli, William Folkner, Kevin Barltrop, Charles Dunn, William Klipstein, Randy Dodge, William Bertch, Daniel Klein, Dong Shin, Stefan Esterhausin, Slava Turyshev, Tom Hoffman, Charles Bell, Hoppy Price, Neil Dahya, Joseph Beerer, Glen Havens, Robert Gounley, Ruth Fragoso, Susan Kurtik, Behzad Raofi, and Dolan Highsmith. From Lockheed Martin Space Systems Company (Denver): Stu Spath, Tim Linn, Ryan Olds, Dave Eckart, and Brad Haack, Kevin Johnson, Carey Parish, Chris May, Rob Chambers, Kristian Waldorff, Josh Wood, Piet Kallemeyn, Angus McMechan, Cavan Cuddy, and Steve Odiorne. From the NASA Goddard Space Flight Center: Frank Lemoine and David Rowlands, and from the University of Texas: Byron Tapley and Srinivas Bettadpur.

References

S. Aoki, H. Kinoshita, Note on the relation between the equinox and Guinot's non-rotating origin. Celest. Mech. **29**, 335–360 (1983)

S. Aoki, B. Guinot, G.K. Kaplan, H. Kinoshita, D. McCarthy, P.K. Seidelmann, The new definition of universal time. Astron. Astrophys. **105**, 359–361 (1982)

D.F. Argus, R.G. Gordon, No-net-rotation model of current plate velocities incorporating plate motion model NUVEL-1. Geophys. Res. Lett. **18**, 2039–2042 (1991)

S.W. Asmar, Radio as a science tool. Proc. IEEE **98**, 10 (2010)

S.W. Asmar, J.W. Armstrong, L. Iess, P. Tortora, Spacecraft Doppler tracking: noise budget and achievable accuracy in precision radio science observations. Radio Sci. **40** (2005). doi:10.1029/2004RS003101

J.G. Beerer, G.G. Havens, Operation the dual-orbiter GRAIL mission to measure the Moon's gravity, in *SpaceOps 2012 Conference*, Stockholm, Sweden, June 2012

C. Boucher, Z. Altamimi, L. Duhem, Results and analysis of the ITRF93. IERS Technical Note, 18, Observatoire de Paris, 1994

C. Dunn, W. Bertiger, Y. Bar-Sever, S. Desai, B. Haines, D. Kuang, G. Franklin, I. Harris, G. Kruizinga, T. Meehan, S. Nandi, D. Nguyen, T. Rogstad, J.B. Thomas, J. Tien, L. Romans, M. Watkins, S.C. Wu, S. Bettadpur, J. Kim, Instrument of GRACE: GPS augments gravity measurements. GPS World **14**, 16–28 (2003)

E.G. Fahnestock, Comprehensive gravity and dynamics model determination of binary asteroid systems, in *American Astronomical Society, DPS Meeting 41, #50.11* (2009)

E.G. Fahnestock, R.S. Park, D.-N. Yuan, A.S. Konopliv, Spacecraft thermal and optical modeling impacts on estimation of the GRAIL lunar gravity field, in *AIAA/AAS Astrodynamics Specialist Conference*, Minneapolis, MN, AIAA, August 13–16, 2012, pp. 2012–4428

R. Floberhagen, P. Visser, F. Weischede, Lunar albedo forces modeling and its effect on low lunar orbit and gravity field determination. Adv. Space Res. **23**, 378–733 (1999)

W.M. Folkner, DSN station locations and uncertainties. JPL TDA Progress Report, 42-128, 1-34, Jet Propulsion Laboratory, California Institute of Technology, Pasadena, CA, 1996

W.M. Folkner, J.A. Steppe, S.H. Oliveau, Earth orientation parameter file description and usage. Interoffice Memorandum 335.1-11-93 (internal document), Jet Propulsion Laboratory, California Institute of Technology, Pasadena, CA, 1993

J. Guinn, P. Wolff, TOPEX/Poseidon operational orbit determination results using global positioning satellites, in *AAS/AIAA Astrodynamics Specialists Conference* (1993). AAS-93-573

S. Hatch, R. Roncoli, T. Sweetser, GRAIL trajectory design: lunar orbit insertion through science, in *AIAA Guidance, Navigation, and Control Conference*, Toronto, Ontario, Canada, August 2010. AIAA 2010-8385

W.A. Heiskanen, H. Moritz, Physical geodesy. Bull. Géod. **86**(1), 491–492 (1967)
T.L. Hoffman, GRAIL: gravity mapping the Moon, in *Aerospace Conference, 2009 IEEE*, Big Sky, MT, 7–14 March 2009. ISBN 978-1-4244-2622-5
W.M. Kaula, *Theory of Satellite Geodesy* (Blaisdell, Waltham, 1966). 124 pp.
J. Kim, Simulation study of a low-low satellite-to-satellite tracking mission. Ph.D. dissertation, Univ. of Texas at Austin, May 2000
J. Kim, B. Tapley, Error analysis of a low-low satellite-to-satellite tracking mission. J. Guid. Control Dyn. **25**(6), 1100–1106 (2002)
W.M. Klipstein, B.W. Arnold, D.G. Enzer, A.A. Ruiz, J.Y. Yien, R.T. Wang, C.E. Dunn, The lunar gravity ranging system for the gravity recovery and interior laboratory (GRAIL) mission. Space Sci. Rev. (2013, this issue)
A.S. Konopliv, S.W. Asmar, E. Carranza, D.N. Yuan, W.L. Sjogren, Recent gravity models as a result of the lunar prospector mission. Icarus **150**, 1–18 (2001)
F.T. Krogh, Changing stepsize in the integration of differential equations using modified divided differences. JPL Tech. Mem. No. 312, Section 914 (internal document), Jet Propulsion Laboratory, California Institute of Technology, Pasadena, CA, 1973
C.L. Lawson, R.J. Hanson, *Solving Least Squares Problems*. SIAM Classics in Applied Mathematics, vol. 15 (Society for Industrial and Applied Mathematics, Philadelphia, 1995)
R. Leavitt, A. Salama, Design and implementation of software algorithms for TOPEX/POSEIDON ephemeris representation, in *AIAA/AAS Astrodynamics Specialists Conference* (1993). AAS-93-724
J.H. Lieske, T. Lederle, W. Fricke, B. Morando, Expressions for the precession quantities based upon the IAU (1976) system of astronomical constants. Astron. Astrophys. **58**, 1–16 (1977)
A.J. Mannucci, B.D. Wilson, D.-N. Yuan, C.H. Ho, U.J. Lindqwister, T.F. Runge, A global mapping technique for GPS-derived ionospheric total electron content measurements. Radio Sci. **33**(3), 565–582 (1998)
D.D. McCarthy, G. Petit (eds.), *IERS Conventions*, IERS Technical Note, vol. 32 (2003)
T.D. Moyer, *Formulation for Observed and Computed Values of Deep Space Network Data Types for Navigation* (Wiley, Hoboken, 2003). 576 pp.
X.X. Newhall, J.G. Williams, Estimation of the lunar physical librations. Celest. Mech. Dyn. Astron. **66**, 21–30 (1997)
R.S. Park, S.W. Asmar, E.G. Fahnestock, A.S. Konopliv, W. Lu, M.M. Watkins, Gravity recovery and interior laboratory simulations of static and temporal gravity field. J. Spacecr. Rockets **49**, 390–400 (2012)
S. Pines, Uniform representation of the gravitational potential and its derivatives. AIAA J. **11**, 1508–1511 (1973)
R. Roncoli, K. Fujii, Mission design overview for the gravity recovery and interior laboratory (GRAIL) mission, in *AIAA Guidance, Navigation, and Control Conference*, Toronto, Ontario, Canada, August 2010. AIAA 2010-8383
P.K. Seidelmann, 1980 IAU theory of nutation: the final report of the IAU working group on nutation. Celest. Mech. **27**, 79–106 (1982)
B.D. Tapley, B. Schutz, G. Born, *Statistical Orbit Determination* (Elsevier, Boston, 2004a). 547 pp.
B.D. Tapley, S. Bettadpur, M. Watkins, C. Reigber, The gravity recovery and climate experiment: mission overview and early results. Geophys. Res. Lett. **31** (2004b). doi:10.1029/2004GL019920
B.J. Thomas, An analysis of gravity-field estimation based on intersatellite dual-1-way biased ranging. JPL Publication 98–15, May 1999
S.G. Turyshev, V.T. Toth, M.V. Sazhin, General relativistic observables of the GRAIL mission. Phys. Rev. D **87**, 024020 (2013)
J.M. Wahr, The forced nutations of an elliptical, rotating, elastic, and oceanless Earth. Geophys. J. R. Astron. Soc. **64**, 705–727 (1981)
R.C. Weber, P.-Y. Lin, E.J. Garnero, Q. Williams, P. Lognonne, Seismic detection of the lunar core. Science **331**, 309–313 (2011). doi:10.1126/science.1199375
J.G. Williams, A scheme for lunar inner core detection. Geophys. Res. Lett. **34**, L03202 (2007). doi:10.1029/2006GL028185
J.G. Williams, D.H. Boggs, W.M. Folkner, DE421 lunar orbit, physical librations, and surface coordinates. JPL IOM 335-JW, DB, WF-20080314-001, March 14, 2008
D.-N. Yuan, W. Sjogren, A. Konopliv, A. Kucinskas, Gravity field of mars: a 75th degree and order model. J. Geophys. Res. **106**(E10), 23377–23401 (2001)
M.T. Zuber, D.E. Smith, D.H. Lehman, T.L. Hoffman, S.W. Asmar, M.M. Watkins, Gravity recovery and interior laboratory (GRAIL): mapping the lunar interior from crust to core. Space Sci. Rev. (2013, this issue). doi:10.1007/s11214-012-9952-7